Lasers in Manufacturing Conference 2017

Deterministic defect generation in selective laser melting: parametric optimization and control

O. Andreau[1,*], P. Peyre[2], J.D. Penot[1], I. Koutiri[2], C. Dupuy[2], E. Pessard[3], N. Saintier[4]

[1] *CEA Saclay DIGITEO Labs Bât. 565 91191 Gif-Sur-Yvette Cedex, France*
[2] *ENSAM Paristech, PIMM, 151 Boulevard de l'hôpital 75013 Paris, France*
[3] *ENSAM Paristech, Lampa, 2 Boulevard du Ronceray, 49100 Angers, France*
[4] *ENSAM Paristech, I2M, Avenue d'Aquitaine 33170 Gradignan, 33400 Talence, France*

Abstract

Selective Laser Melting (SLM) is a powder based additive manufacturing process where parts are made layer-by-layer from a 3D file (STL). The complexity of a part is not a barrier in SLM, and thus the process opens new doors to design and elaborate intricate and complex shapes. This study focuses on the deterministic defect/pore generation SLM –i.e. leaving precisely unmelted powder zones in an SLM part on purpose. In order to get a high accuracy and part reproducibility, a thorough parametric optimization is required, especially for the laser contour scan, which determines both the roughness outside a part and the geometry inside a deterministic defect. Different sets of parameters must be used for the contour and hatch scans, in order to obtain a minimum porosity amount in the solid area while getting a minimal deformation around the pores. The deterministic pore generation gives new tools to characterize and develop new NDT techniques or simulate casting defects. Those pores could also be integrated in novel multifunctional materials, to implement damage detection (structural health monitoring) or to attain better thermal properties while still keeping good mechanical performances.

Keywords: SLM; Contour; Pore; Defect; NDT

1. Introduction

In additive manufacturing (AM) processes, materials' layers are successively added to generate objects from 3D data, known as STL files. It is opposed to traditional manufacturing which usually uses subtraction on a bulk part. Among AM processes, powder bed fusion (PBF) processes can create metallic parts from metal or alloy powders. The SLM process (Selective Laser melting) is one of the most common PBF process and has been developed extensively for the last two decades. (Wohlers 2016; Meiners et al. 1999).

* Corresponding author.
E-mail address: olivier.andreau@cea.fr

SLM consists in successively melting powder layers on top of each other with a laser, following a pattern indicated by a 3D STL file. This technique offers high design freedom and needs little to no post-processing machining. New and innovative parts can be made, such as porous, lattice and scaffold structures (Heinl et al. 2008) for bio-medical application, topology optimization or providing dedicated mechanical behavior (Alsalla et al. 2016).

Pores inside dense SLM parts are usually avoided by using the correct set of parameters for laser irradiation (power P, scan speed V, spot diameter D) and scan strategy (Kruth et al. 2004; Thijs et al. 2010; Kruth et al. 2010). These defects can have several sources: lack of fusion (Gong et al. 2014), metal evaporation in keyhole mode, (King et al. 2014), spatter ejection (Mumtaz & Hopkinson 2010), or even argon entrapped in the metal powder during the atomization process (Biamino et al. 2011). The impact of these defects on mechanical properties has been investigated already (Haijun Gong et al. 2012; Leuders et al. 2014; Riemer et al. 2014).

It is known that pores can greatly impact the endurance of a part in fatigue. However, acquiring and machining samples with localized defects with traditional methods such as casting is challenging, making the experimental confirmation difficult. Selective laser melting offers a new way to generate deterministic defects or internal pores to experimentally simulate real defects in mechanically-tested parts.

Little investigation has been conducted on the deterministic defects implementation in SLM and their mechanical influence in dense parts, i.e. pores that are added on purpose in the part using the 3D file (Gong 2013; Fadida et al. 2015). Manufacturing internal deterministic defects with no supporting requires to control precisely the melt pool on overhanging surfaces (Clijsters et al. 2012; Kruth et al. 2007; Calignano 2014). Since the heat conduction is much lower on powder supported zones than on solid supported zones, the melt pool will become much larger and sink into the powder with gravity and capillary forces (Calignano 2014). The staircase effect will also affect the curvature and the general aspect of curved surfaces because of the slicing of the 3D file. Fig. *1* illustrates the staircase effect due to the slicing of an internal pore in a CAD file. The contour offset is not shown in the figure, but is a crucial parameter in order to take into account the melt pool width in the laser contour track calculation. The positioning in height of the pore itself modulo the layer thickness, and its mesh in the CAD file can also impact its final shape.

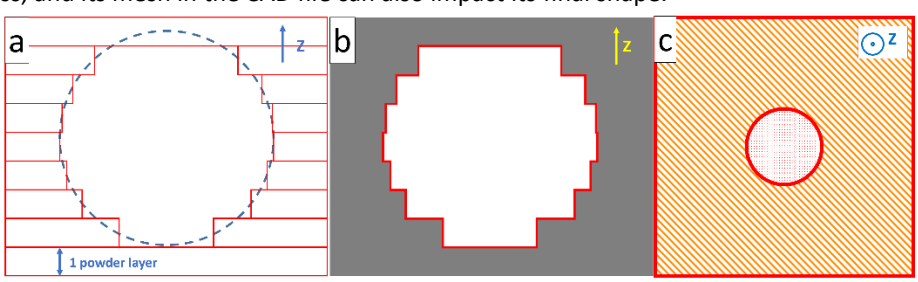

Fig. 1. (a) X-Z slicing of a spherical pore in a CAD file, (b) resulting calculated contour inside the dense part, (c) X-Y view of one slice with the contour (red) and hatch (orange)

There are more than a hundred variables for the laser scanning strategy and parametrization, not including some additional parameters, such as powder granulometry, shape, or even the time between successive layers. Among all the laser parameters, contour and hatching scanning parameters appear to have the highest influence for an internal pore generation. Contour and hatching are described Fig. *1*. While hatching fills the “bulk” area of a part, the contour will outline the limit between the dense part and unmelted powder. Different (P, V, D) laser parameters can be set for the hatching or the contour.

In this study, the feasibility of sub-millimetric deterministic spherical defect generation has been investigated on a stainless steel (316L). The goal behind the fabrication of those pores is to provide a new way of validating high cycle fatigue models and criteria. This work aims to describe the influence of some key variables and parameters to generate spherical and reproducible deterministic pores inside dense parts.

2. Material and methods

2.1. Samples and methods

The machine used in this work was a SLM 125 HL (SLM Solutions GmbH) with a minimum spot size of 70 µm and a maximum laser power of 400 W. For each layer, the laser scans the desired pattern of the CAD file. Then, the building platform moves down from 30 µm and the process is repeated until the final part is finished. All the excess powder collected is then recycled for other tests. It has been observed that sieved recycled powder does not have a negative impact on part quality (Ardila et al. 2014). The 316L powder was plasma atomized in the range of 17 to 51 µm with a median peak at 29.44 µm.

In order to characterize defects in metallography, different sample morphologies have been used (Fig. *2*):

- Square based with 4 egg-shaped pores of different sizes elongated along the Y-axis: model I
- Square based with 4 egg-shaped pores of the same size elongated along the Y-axis: model II

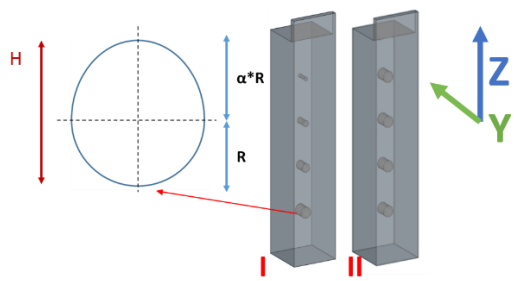

Fig. 2. Samples fabricated by SLM and close-up on a pore section

The samples have their pores elongated along the Y-axis for 1 millimeter (like cylinders) in order to ease their observation after grinding polishing and make sure they were observed at their maximum dimensions. All pores' upper half was elongated with a factor α=1.2 (egg-shaped configuration) in order to compensate slightly for melt pool collapse and minimize the near-horizontal overhanging area.

Four pore sizes have been chosen and their sections' dimensions are shown in Table 1.

Table 1. Pore dimensions in the CAD file

Sample	Pore 1	Pore 2	Pore 3	Pore 4
Width (µm)	900	710	490	300
Height (µm)	990	781	539	330

Constant hatching parameters were used: 200 W, 700 mm/s, with a 100 µm hatch. The parameters for contour scanning used for the investigation are shown in Table 2. Volumetric Energy Density (VED) is calculated with the following formula:

(1)

$$VED\ (J/m^3) = \frac{\mathrm{P\ (W)}}{\mathrm{S\ (m^2)} * \mathrm{V}(m/s)}$$

With S the laser spot area

Table 2. Model I samples parametrization. Samples in bold were repeated twice: with model II and lower VED hatching strategy.

Sample	Speed (mm/s)	Power (W)	VED (J/mm^3)
A	400	100	65
B	400	140	90
C	400	180	117
D	**400**	**220**	**143**
E	400	260	169
F	500	100	52
G	**500**	**140**	**73**
H	**500**	**180**	**94**
I	500	220	114
J	500	260	135
K	600	100	43
L	**600**	**140**	**61**
M	600	180	78
N	600	220	95
O	600	260	113
P	**700**	**100**	**37**

The 16 model I samples have been fabricated with two laser scanning order strategies: contour-hatching and hatching-contour, which makes a total of 32 samples.

In addition to the 32 samples, the samples D, G, H, L, and P in bold (Table 2) were repeated for each of the following modifications:

- With a lower energy hatching strategy = 185 W, 800 mm/s, 100 µm hatch
- Considering model II samples for addressing the effect of building height

A total of 42 samples have been fabricated for the experiment, and have been mounted and polished to reveal the pores after fabrication. The pores were then observed with a Zeiss Imager M2m optical microscope and the images were acquired with a 5 Megapixels Zeiss Icc5 camera at magnifications x 100 and x 200, depending on the pore size.

2.2. Image processing

In order to evaluate systematically the morphology of the pores from microscopy pictures, an automatic image processing method has been developed (Fig. *3*). The method includes the following steps:

- Metadata extraction of the scale from the microscopy picture
- Gaussian blur to remove artifacts and binarization of the images (pores in white, bulk in black)
- Detection of the biggest pore present in the image and measurement of the pore area/perimeter
- Fit of the pore by an ellipse that has the same normalized second central moments as the pore
- Extraction of the data and conversion in µm (Height, width of the fitted ellipse, pore area, perimeter, circularity)

Fig. 3. Image processing of a pore

3. Results and discussion

3.1. Porosity and mechanical behaviour

In order to be viable, deterministic pore fabrication requires a dense bulk with few or no undesired pores in the bulk of the part. Indeed, if we want to observe clearly the mechanical role of a deterministic pore inside a sample, it should have a minimum amount of defects elsewhere that could impact its mechanical behavior. Porosity has been measured using image processing on 20 images taken at x100 magnification in bright field with an optical microscope. Results shown in Fig. *4* for the two hatching parameters (contour energy densities E between 61 and 94 J/mm^3) indicate porosity rates of 0.075 % and 0.04 %. These values are in accordance with the literature. (Kamath et al. 2014) The tensile tests were carried out at 5*10^{-4} s^{-1} and 200 W-800 mm/s (65 J/mm^3) conditions. The average maximum strength was 706 ±17 MPa, which is around the upper limit found in the literature for tensile strength of 316L SLM build parts (Zhang et al. 2013)**.** The maximum strain was found to be at least 45 %, two of the three samples did not break before reaching the extension limit of the extensometer.

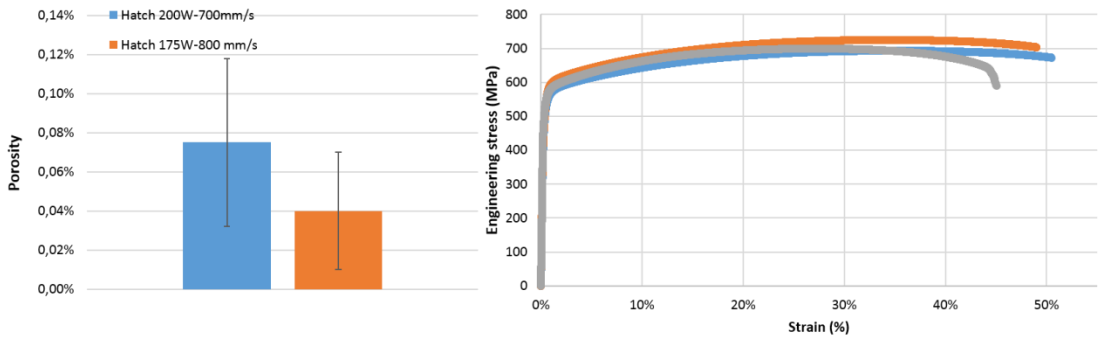

Fig. 4. Porosity rates and tensile tests on 316L samples

3.2. Laser scanning order and resulting pore shape

After fabricating the set of samples (Table 2) for the two laser scanning orders, and mounting + polishing the samples, the heights of the pores have been measured. The smallest pores (330 µm height) could not be observed for the samples scanned with the hatching-contour order. The difference in height with the CAD model is displayed Fig. *5*. The contour energy volumetric density does not seem to have any impact on the difference in height with the model. The pore size has no impact on that difference either: the gap is constant. It has been averaged at 150 ± 75 µm for contour-hatching and 335 ± 60 µm for hatching contour.

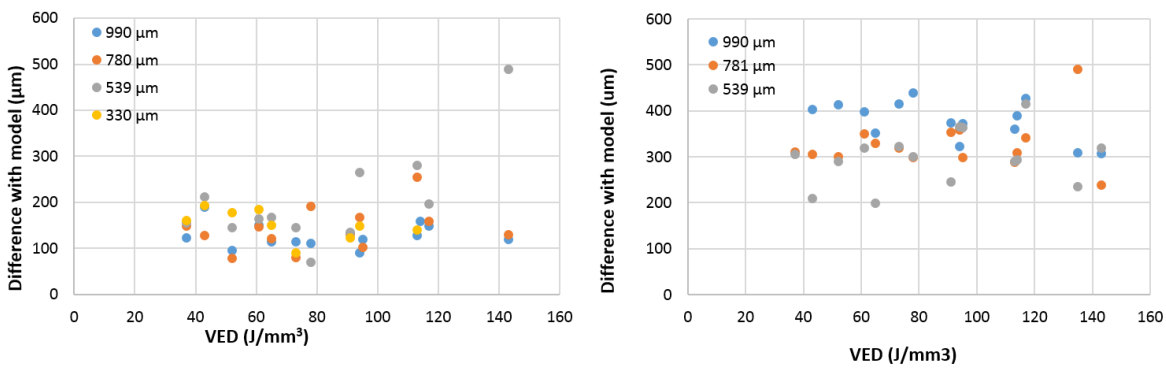

Fig. 5. Difference in height with the CAD model (left) for contour-hatching (right) for hatching-contour

It can be assumed that the collapse is more important in the pores carried out for the hatching contour order because of the higher average temperature of the part T_0 before the contour is made. This is mostly due to the significantly longer hatching stage (and resulting accumulated energy) than the contour stage, thus contributing predominantly to the average temperature rise. In the hatching-contour configuration, as soon as the hatching stage is completed on all the parts, the laser starts the contour. As a result, the material has no time for thermal dissipation, and the melt pool is larger and deeper than in contour-hatching where the material has been cooled down by the powder spreading and a longer dissipation time after the hatching step. Consequently, more collapse is evidenced on overhanging areas for the hatching-contour order because of larger melt-pool volumes for similar energies E, as illustrated on Fig. *6*. The bottom of the hatching-contour samples is flatter, while the geometry on the top is largely impacted by melt pool collapse.

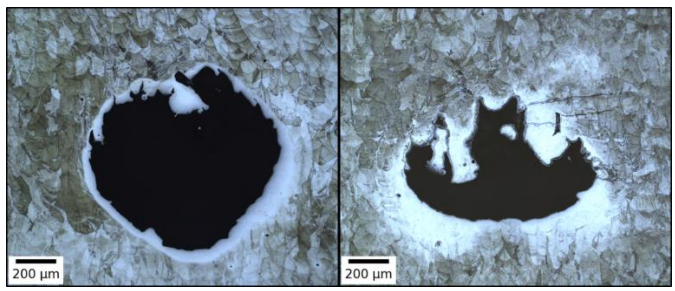

Fig. 6. Etched sample C, 990 µm pore observed in an optical microscope in bright field for contour hatching (left) and hatching contour (right)

3.3. Impact of hatching parametrization

The 5 samples in bold (Table 2) have been repeated with a low energy hatching condition E=57 J/mm^3 instead of 74 J/mm^3 for the first test. Fig. *7* displays the height of the pores versus the volumetric energy density of the contour for both hatchings. For each pore size and contour energy density, results are shown with low hatching energy density (disk) and high hatching energy density (cross). Once again, no effect of the contour energy density is observed on the pore height. However, an almost systematic gap in height is observed between high hatching energy and low hatching energy pores. It appears that a higher hatching energy density leads to a higher collapsing effect inside the pores, and impacts their dimensions.

In order to illustrate the effect of hatching conditions on pore geometry, some samples have been etched and observed with an optical microscope in dark field mode. Measurements indicate a bead depth of 160-220 µm, which goes 130-190 µm into the previous layers (Fig. *8*). Those measurements are in accordance with the height difference observed on Fig. *5* (left).

To understand dimensional instabilities of overhanging contours, one can consider pressures applied on melt-pools, which directly affects its shape and flow:

- Gravitational pressure is applied on the overhanging melt pool (over the un-melted powder):

$$P_L = \rho * g * h \quad (2)$$

With h the height of the melt pool, ρ the volumetric mass density, g the gravitational constant

- Capillary pressure P_c prevents the melt pool flow with its surface tension:

$$P_c \propto \frac{\eta}{R} \quad (3)$$

With η≈1.7N.m^{-1} the surface tension of the melt pool tip, R the spot radius (≈50µm)

- Recoil momentum pressure P_r applied over a surface of temperature T by the saturated vapor (Bäuerle 2011) contributes to melt-pool collapse.

(4)

$$Pr = 0.56 * P^{*} e^{\left[\frac{\lambda}{k_B}*\left(\frac{1}{T_b}-\frac{1}{T}\right)\right]}$$

With λ=4.3eV the evaporation energy per atom, k_B=8.62.10^{5} eV.K^{-1} the Boltzmann constant, P*=ambient pressure, T_b=3086 K the boiling temperature of 316L.

While gravitational pressures appear to be 2 orders of magnitude below capillary forces, recoil pressure exceeds capillary forces. This correlates with the aspect ratio of the melt pool (width/depth >1 on Fig. *8*) that indicates a keyhole mode, where the melt pool depth is driven by recoil pressure. (Khairallah et al. 2016)**.** The W/D ratio of the melt pool around the pore must be kept around or below 1 at the overhang zones (conduction mode) by minimizing the VED input, in order to decrease the melt pool collapse.

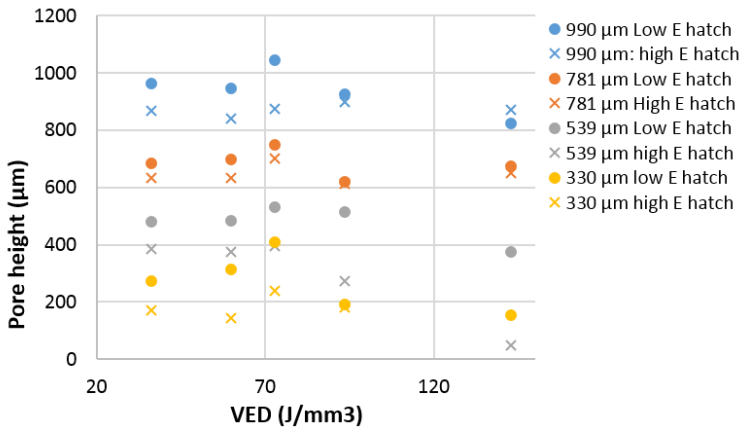

Fig. 7. Pore height VS contour energy density for two different hatching energy densities (contour-hatchning order)

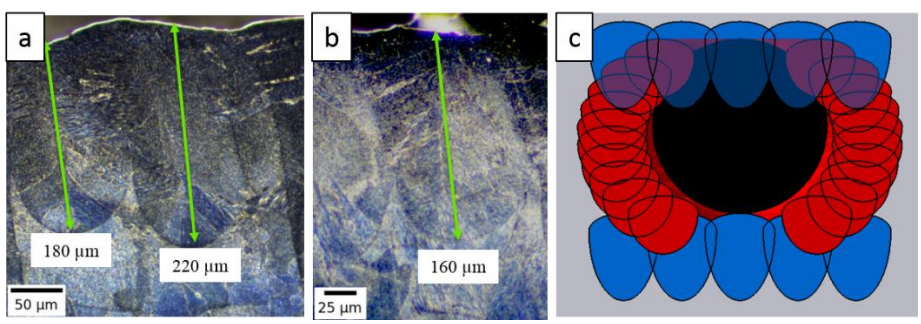

Fig. 8. (a,b): hatching scan depth measured for a 200W and 700 mm/s parametrization. (c): X-Z Cross section of a schematic laser scans visualisation for a spherical pore of 300µm diameter with contour tracks(red) and hatching tracks (blue)

The relation between melt pool dimensions and process conditions has been widely discussed in previous works (Kamath et al. 2014; Yadroitsev et al. 2010; Yadroitsev et al. 2013) and the present work confirms that energy density, and thus average temperature, must be minimized when possible to decrease the molten track depth at the overhang areas above the pores.

3.4. Fabrication height and pore reproducibility

Samples model II with 4 identical pores repeated along the Z axis have been built with the lasing parameters in bold Table 2. Their circularity c, height and width have been measured. Circularity was calculated with the following formula:

(5)

$$c = \frac{p^2}{4 * \pi * A}$$

With p the pore perimeter, and A the area of the pore.

The four pores are placed at 4, 8, 12 and 16 mm height in the sample. The sample itself is placed at 3 mm above the build plate and is attached on it with a grid support. After fabrication, it is removed from the plate, ground and polished until the pores inside are observable. Height and width are then used to calculate the ratio H/W that should reach 1 for a perfectly circular pore, just like circularity.

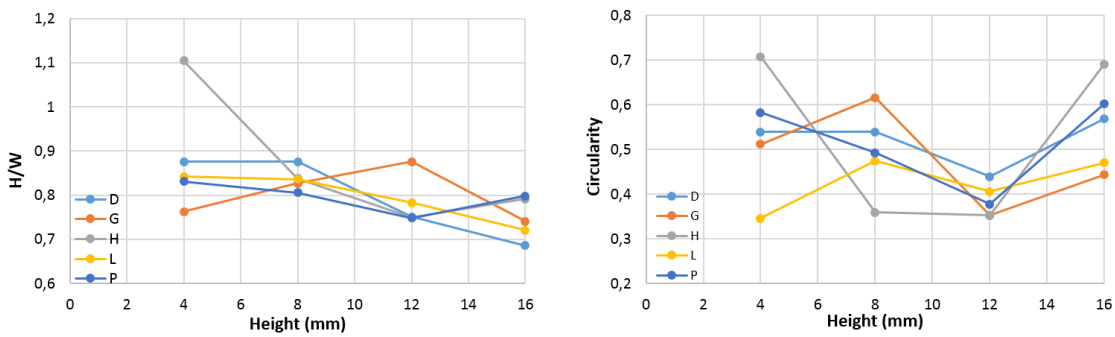

Fig. 9. (Left) height/Width ratio VS height in Z, (right) circularity VS height in Z

Both H/W ratio and circularity tend to decrease between 4 and 12 mm heights (see

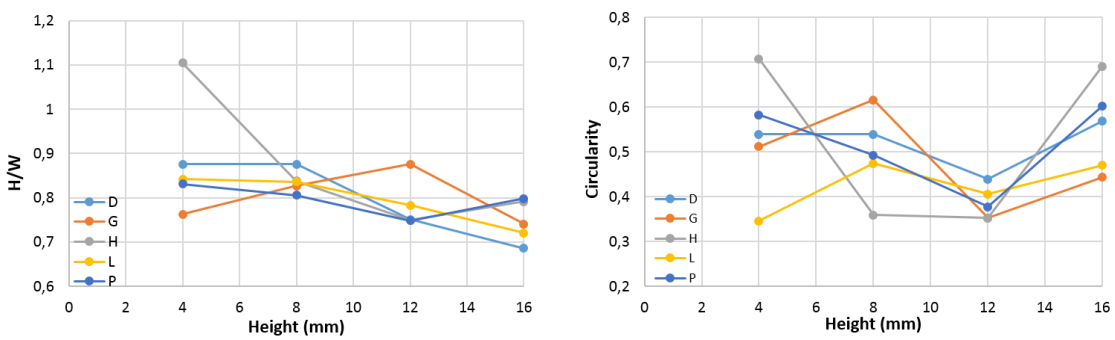

Fig. *9*). It can indeed be seen from Fig. *10* that the height of the pores decreases while the width stays constant, hence decreasing the H/W ratio. However, H/W continues to go down above 12 mm while circularity goes back up.

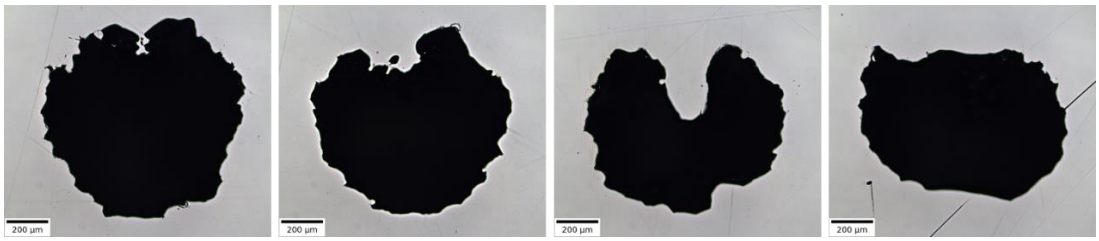

Fig. 10. (From left to right) pores in Sample H, at 4, 8, 12 and 16 mm height

With the successive laser tracks, the upper layers tend to reach a higher T_0 local temperature (Roberts et al. 2009; Foroozmehr et al. 2016). As a result, the melt pool volume tends to grow in upper layers since the volumetric energy required to melt the material is inferior. A larger melt pool will then collapse more, resulting in a decrease of H/W ratio with increasing Z. The increase in circularity on the last pore (at 16 mm height) of every sample is linked to the increase in melt pool volume that flattened the top of the pore. Since the whole top of the pore is flat, its perimeter is reduced, leading to a higher circularity for a pore that is far from being round. The H/W ratio should be seen as a first order criterion for sphericity, while the circularity comes as a second order criterion to reflect the "roughness" inside the pore.

Once again, this result traduces the overall importance of process parameters and resulting local average temperatures T_0 (x,y,z). High T_0 (x,y,z) promotes larger and more unstable melt-pools on overhanging surfaces which enlarge fusion isotherms and favor melt-pool collapse.

4. Conclusion

Through the analysis of 316L stainless steel samples containing deterministic pores in 316L, some key parameters and conditions necessary for the fabrication of internal spherical pores were identified.

i) The scanning order is crucial when fabricating parts with overhang areas and no supports. It appears that doing the contour before the bulk hatching reduces the dross effect and melt pool collapse in overhang areas.

ii) Low energy (i.e. low power, high speed) hatching must be privileged in overhang areas above the pores, in order to minimize the melt pool depth and stay close to the CAD model.

iii) A thermal gradient along the building axis was indirectly observed by looking at the pore geometry. Reducing the volumetric energy density via the laser parametrization or increasing the time between layers recoating should lower the temperature of the part and give it more time to cool down between layers.

References

Alsalla, H., Hao, L. & Smith, C., 2016. Fracture toughness and tensile strength of 316L stainless steel cellular lattice structures manufactured using the selective laser melting technique. *Materials Science and Engineering A*, 669, p.1–6.

Ardila, L.C. et al., 2014. Effect of IN718 recycled powder reuse on properties of parts manufactured by means of Selective Laser Melting. *Physics Procedia*, 56(C), p.99–107.

Bäuerle, D., 2011. *Laser Processing and Chemistry*, Springer.

Biamino, S. et al., 2011. Electron beam melting of Ti-48Al-2Cr-2Nb alloy: Microstructure and mechanical properties investigation. *Intermetallics*, 19(6), p.776–781.

Calignano, F., 2014. Design optimization of supports for overhanging structures in aluminum and titanium alloys by selective laser

melting. *Materials and Design*, 64, p.203–213.

Clijsters, S., Craeghs, T. & Kruth, J.P., 2012. A priori process parameter adjustment for SLM process optimization. *Innovative Developments in Virtual and Physical Prototyping - Proceedings of the 5th International Conference on Advanced Research and Rapid Prototyping*, p.553–560.

Fadida, R., Rittel, D. & Shirizly, A., 2015. Dynamic Mechanical Behavior of Additively Manufactured Ti6Al4V With Controlled Voids. *Journal of Applied Mechanics*, 82(4), p.41004.

Foroozmehr, A. et al., 2016. Finite Element Simulation of Selective Laser Melting process considering Optical Penetration Depth of laser in powder bed. *Materials and Design*, 89, p.255–263.

Gong, H. et al., 2014. Analysis of defect generation in Ti-6Al-4V parts made using powder bed fusion additive manufacturing processes. *Additive Manufacturing*, 1, p.87–98.

Gong, H., 2013. Generation An Detection Of Defects In Metallic Parts Fabricated By Selective Laser Melting And Electron Beam Melting And Their Effects On Mechanical Properties. *University of Louisville*.

Haijun Gong, Khalid Rafi, Thomas Starr, B.S., 2012. EFFECT OF DEFECTS ON FATIGUE TESTS OF AS-BUILT TI-6AL-4V PARTS FABRICATED BY SELECTIVE LASER MELTING Haijun. , 1, p.499–506.

Heinl, P. et al., 2008. Cellular Ti-6Al-4V structures with interconnected macro porosity for bone implants fabricated by selective electron beam melting. *Acta Biomaterialia*, 4(5), p.1536–1544.

Kamath, C. et al., 2014. Density of additively-manufactured, 316L SS parts using laser powder-bed fusion at powers up to 400 W. *International Journal of Advanced Manufacturing Technology*, 74(1–4), p.65–78.

Khairallah, S.A. et al., 2016. Laser powder-bed fusion additive manufacturing: Physics of complex melt flow and formation mechanisms of pores, spatter, and denudation zones. *Acta Materialia*, 108, p.36–45.

King, W.E. et al., 2014. Observation of keyhole-mode laser melting in laser powder-bed fusion additive manufacturing. *Journal of Materials Processing Technology*, 214(12), p.2915–2925.

Kruth, J. et al., 2007. Feedback control of Selective Laser Melting. *Proceedings of the 3rd International Conference on Advanced Research in Virtual and Rapid Prototyping*, p.1–7.

Kruth, J. et al., 2010. Part and material properties in selective laser melting of metals. *16th International Symposium on Electromachining*, p.1–12.

Kruth, J.P. et al., 2004. Selective laser melting of iron-based powder. In *Journal of Materials Processing Technology*. p. 616–622.

Leuders, S. et al., 2014. On the fatigue properties of metals manufactured by selective laser melting – The role of ductility. *Journal of Materials Research*, 29(17), p.1911–1919.

Meiners, W. et al., 1999. Direct Generation of Metal Parts and Tools by Selective Laser Powder Remelting (SLPR). *Proc. Solid Freeform Fabrication Symposium*, p.655–661.

Mumtaz, K.A. & Hopkinson, N., 2010. Selective Laser Melting of thin wall parts using pulse shaping. *Journal of Materials Processing Technology*, 210(2), p.279–287.

Riemer, A. et al., 2014. On the fatigue crack growth behavior in 316L stainless steel manufactured by selective laser melting. *Engineering Fracture Mechanics*, 120, p.15–25.

Roberts, I.A. et al., 2009. A three-dimensional finite element analysis of the temperature field during laser melting of metal powders in additive layer manufacturing. *International Journal of Machine Tools and Manufacture*, 49(12–13), p.916–923.

Thijs, L. et al., 2010. A study of the microstructural evolution during selective laser melting of Ti-6Al-4V. *Acta Materialia*, 58(9), p.3303–3312.

Wohlers, T., 2016. *Wohlers Report 2016. 3D Printing and Additive Manufacturing State of the Industry*,

Yadroitsev, I. et al., 2013. Energy input effect on morphology and microstructure of selective laser melting single track from metallic powder. *Journal of Materials Processing Technology*, 213(4), p.606–613.

Yadroitsev, I. et al., 2010. Single track formation in selective laser melting of metal powders. *Journal of Materials Processing Technology*, 210(12), p.1624–1631.

Zhang, B., Dembinski, L. & Coddet, C., 2013. The study of the laser parameters and environment variables effect on mechanical properties of high compact parts elaborated by selective laser melting 316L powder. *Materials Science and Engineering A*, 584, p.21–31.